

## The deposition angle-dependent density of amorphous solid water films

Z. Dohnálek, Greg A. Kimmel, Patrick Ayotte, R. Scott Smith, and Bruce D. Kay

Citation: *The Journal of Chemical Physics* **118**, 364 (2003); doi: 10.1063/1.1525805

View online: <http://dx.doi.org/10.1063/1.1525805>

View Table of Contents: <http://scitation.aip.org/content/aip/journal/jcp/118/1?ver=pdfcov>

Published by the AIP Publishing

---

### Articles you may be interested in

Response to "Comment on 'Mixture model description of the T-, P dependence of the refractive index of water'" [J. Chem. Phys. **115**, 7795 (2001)]

J. Chem. Phys. **115**, 7796 (2001); 10.1063/1.1406530

Comment on "Mixture model description of the T-, P dependence of the refractive index of water" [J. Chem. Phys. **114**, 3157 (2001)]

J. Chem. Phys. **115**, 7795 (2001); 10.1063/1.1406529

Simultaneous measurement of changes in thickness and refractive index of weakly absorbing self-standing solid films using optical interferometry

Rev. Sci. Instrum. **72**, 2842 (2001); 10.1063/1.1372676

Mixture model description of the T-, P dependence of the refractive index of water

J. Chem. Phys. **114**, 3157 (2001); 10.1063/1.1331571

Density and index of refraction of water ice films vapor deposited at low temperatures

J. Chem. Phys. **108**, 3321 (1998); 10.1063/1.475730

---



Launching in 2016!  
The future of applied photonics research is here

AIP | APL  
Photonics

# The deposition angle-dependent density of amorphous solid water films

Z. Dohnálek, Greg A. Kimmel, Patrick Ayotte, R. Scott Smith, and Bruce D. Kay<sup>a)</sup>

*Pacific Northwest National Laboratory, Environmental Molecular Sciences Laboratory,  
Richland, Washington 99352*

(Received 2 August 2002; accepted 7 October 2002)

The index of refraction and thickness of amorphous solid water (ASW) films are determined using laser optical interferometry. From the film thickness, the density of ASW can be calculated directly since the molecular beam flux and the H<sub>2</sub>O condensation coefficient are both known. From the index of refraction the ASW density can also be determined using the Lorentz–Lorenz relationship. The densities determined via both methods agree within experimental uncertainty. For films deposited at 22 K using a collimated molecular beam, the index of refraction and density decrease monotonically as the deposition angle is varied from normal to oblique incidence. At normal incidence the films have an index of refraction of 1.285 and are presumed to be fully dense (0.94 g/cm<sup>3</sup>). At glancing incidence (86°) the film has a refractive index of 1.05 and a density of 0.16 g/cm<sup>3</sup>, indicating a porosity exceeding 80%. The angle-dependent film density is in semiquantitative agreement with the results of ballistic deposition simulations of ASW film growth. © 2003 American Institute of Physics. [DOI: 10.1063/1.1525805]

## I. INTRODUCTION

Amorphous solid water (ASW) is formed by deposition of water vapor on cold substrates at temperatures less than ~130 K. The absence of long-range order is related to the limited surface mobility of the water molecules at such low deposition temperatures, and this limited mobility can also result in the growth of porous films.<sup>1–3</sup> The factors that determine the morphology of ASW films, such as deposition temperature and flux, have been the subject of numerous investigations.<sup>2–9</sup> Recently, we have also shown that the angular distribution of the impinging water molecules can dramatically influence the ASW film morphology.<sup>2,3</sup>

For films grown at low temperatures where surface diffusion is limited, the particles (atoms, molecules) will be incorporated into the film at or very near the site where they initially strike the film—often referred to as “hit and stick” film growth.<sup>10</sup> In this case, the stochastic nature of the deposition process will lead initially to the formation of a rough surface. The subsequent development of the film morphology is largely dependent on the angle of incidence of the particles from the gas phase: For normal and nearly normal angles of incidence, particles from the gas phase can reach most of the surface of the film and the resulting films are dense. For large angles of incidence, the high points in the film intercept a larger flux of the particles from the gas phase and thus cast “shadows” over the regions behind them on the surface (i.e., regions of low particle flux). Since the length of the “shadow” is proportional to  $\tan \theta$ , the shadowing effect is a sensitive function of deposition angle for large  $\theta$ . Furthermore, since the high points in the film differentially intercept a higher portion of the particle flux, they grow faster and the process is self-reinforcing. The shadowing effect results in

the formation of tilted columns with voids in between.<sup>11–13</sup>

In this study, we report on the density of ASW films measured with laser interferometry during the film growth for a variety of different deposition angles. The index of refraction and the thickness of the film can be used to extract the ASW film density from the reflectance measurements.<sup>5,9</sup> These results yield information about the morphology of ASW films that is complementary to our previous measurements of their surface area.<sup>2,3</sup> The angle-dependent densities determined in this study are compared with the results of ballistic deposition simulations.<sup>1</sup>

## II. EXPERIMENT

The experiments were conducted in an ultrahigh vacuum (UHV) molecular beam surface scattering apparatus having a base operating pressure of  $1 \times 10^{-10}$  Torr. The ASW films for the laser interferometry measurements were grown on an oxidized Mo(100) crystal. The surface area measurements were performed on ASW films deposited on clean Pt(111) as described previously.<sup>2,3</sup> The substrates were mounted on a closed-cycle He cryostat that, in conjunction with resistive heating, allowed temperature control from 22 to 1600 K. The sample temperature was measured using tungsten–rhenium (type C) and chromel–alumel (type K) thermocouples on oxidized Mo(100) and clean Pt(111) substrates, respectively. In each case, an absolute temperature calibration was performed by monitoring the desorption of rare gas multilayers.<sup>14</sup> The oxidized Mo(100) substrate was prepared by annealing at 1500 K in a background of O<sub>2</sub> ( $1 \times 10^{-6}$  Torr). The Pt(111) substrate was cleaned using a sequence of Ne<sup>+</sup> sputtering at 22 K, O<sub>2</sub> annealing at 1200 K ( $2 \times 10^{-7}$  Torr), and UHV annealing at 1300 K. These cleaning procedures remove trace amounts of carbon as observed via Auger electron spectroscopy (AES).

Thin ( $\leq 1 \mu\text{m}$ ) ASW films were deposited at 22 K using

<sup>a)</sup>Author to whom correspondence should be addressed. Electronic mail: bruce.kay@pnl.gov

a quasieffusive molecular beam<sup>15</sup> of H<sub>2</sub>O at different angles of incidence,  $\theta$ , with respect to the substrate normal. An H<sub>2</sub>O beam having a flux of  $2.3 \times 10^{14}$  molecules/cm<sup>2</sup>/s at normal angle of incidence was used, yielding an angle-dependent deposition rate of  $2.3 \times 10^{14} \times \cos \theta$  molecules/cm<sup>2</sup>/s. The angular divergence of the H<sub>2</sub>O beam at the sample is FWHM  $\sim 0.4^\circ$ . A second dosing method involved introduction of H<sub>2</sub>O vapor into the system via a leak valve providing a flux of molecules on the substrate with a cosine distribution. Since this “background deposition” technique is frequently used, it provides an important comparison with the films grown with a collimated beam of water molecules. For the experiments reported here the background dosing flux was  $\sim 10^{14}$  H<sub>2</sub>O/cm<sup>2</sup>/s.

The surface area of the ASW films was characterized using the adsorption of weakly bound gases such as N<sub>2</sub>, Ar, and CH<sub>4</sub>.<sup>2,3,16</sup> The gases were deposited using a pure, 300 K supersonic beam that was smaller than and centered on the ASW film. Temperature programmed desorption (TPD) experiments used a linear ramp rate of 0.6 K/s. The adsorbed, desorbed, and reflected fluxes were measured in an angle-integrated fashion using a quadrupole mass spectrometer (QMS).

The optical reflectance of the ASW film/substrate was measured during the film growth using a laser interference technique. In this setup, a linearly polarized HeNe laser (632.8 nm) is reflected from the film/substrate. The intensity of the specularly reflected beam was measured using a photodiode. In general, the amplitude of the reflected wave,  $R$ , can be described using the following relationship:<sup>17</sup>

$$R = \frac{r_1 + r_2 \exp(-i2\delta_1)}{1 + r_1 r_2 \exp(-i2\delta_1)}. \quad (1)$$

Here,  $r_1$  and  $r_2$  are the Fresnel coefficients which are functions of the optical properties (index of refraction and extinction coefficient) of the film and the substrate, and  $\delta_1$  is the optical phase thickness of the film. Since  $R$  is a complex variable, the measurable value of specular reflectance,  $\mathbf{R}$ , is obtained by evaluating  $\mathbf{R} = |R|^2$ .

Geometric constraints imposed by the molecular beam and the vacuum chamber layout required that the reflectance measurements be made at various incident laser beam angles,  $\varphi_0$ . This complicates the conceptually simple analysis of the reflectance data as outlined in many textbooks.<sup>17</sup> Unfortunately, we were unable to find a published solution for the general case of a film on an absorbing substrate measured at off-normal angles of incidence (schematically shown in Fig. 1). The explicit solution for this general case with a film thickness,  $z$ , indexes of refraction,  $n$  and  $n_s$ , and extinction coefficients,  $k$  and  $k_s$ , of the film and the substrate, respectively, is provided in the Appendix.

### III. SIMULATIONS

The details of the ballistic deposition simulations have been given previously.<sup>1</sup> Therefore, we will only briefly review the ballistic deposition simulations that are used to model the growth of porous ASW films. The basis for the

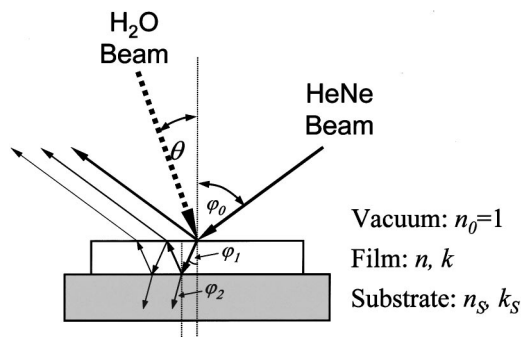


FIG. 1. Schematic of the optical interference experiment during the growth of ASW films on an oxidized Mo(100) substrate.

ballistic deposition model is that at low surface temperatures—temperatures well below the melting point—surface diffusion is often slow compared to the rate at which particles arrive from the vapor phase.<sup>10</sup> In this case, the structure of the growing film will be strongly influenced by the deposition geometry and the randomness inherent in the deposition process. Other factors such as the bonding geometry in the film will also play a role, but many of the qualitative features of the mesoscopic structure of the films can be investigated with relatively simple simulations.

For the ballistic deposition simulations presented here, the film consists of particles in a three-dimensional cubic lattice with periodic boundary conditions in the two lateral dimensions. The initial starting points for the incident particles above the surface are randomly chosen. The particles follow straight-line trajectories and stick at the first point in the film they strike.<sup>1,18</sup> After the particle initially hits the surface, it can be allowed to move to find a more highly coordinated configuration, i.e., the films can be “annealed.” Several simple algorithms have been used to anneal the films, and the results are qualitatively independent of the algorithm used. Annealing the films allows us to investigate, in a qualitative manner, the stability of the film structure to “diffusive-like” motion that is expected to lead to smoothing and densification. The details of the annealing procedure have been published elsewhere.<sup>1</sup>

Simulations were performed with two different angular distributions for the incident particles. The first type has “collimated beams” in which every particle has the same incident angle. These simulations correspond to experiments where the films are grown with a molecular beam. We also ran simulations in which the particles’ incident angle was randomly chosen from a cosine distribution of polar angles,  $\theta$ , and an isotropic distribution of azimuthal angles. These “background dosing” simulations correspond to experiments in which the ASW films were grown by introducing water vapor into the chamber through a leak valve.

### IV. RESULTS AND DISCUSSION

For all the experiments reported here, the optical reflectance is measured as a function of time,  $t$ , during the film growth. However, since the oscillation periods are quite dif-

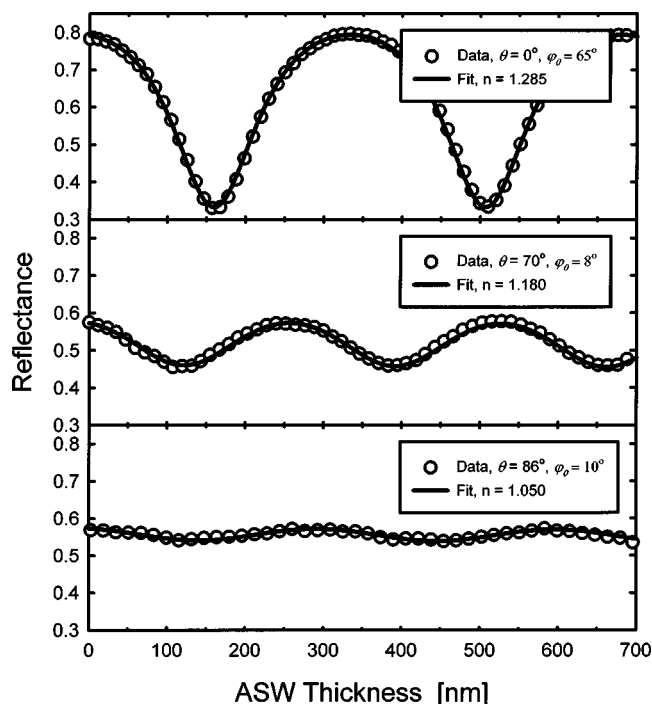


FIG. 2. Optical interferograms obtained during the growth of ASW films on oxidized Mo(100) at 22 K and different deposition angles,  $\theta$ . The solid lines represent the solution of Eq. (1) with film thickness and index of refraction as fitting parameters.

ferent for the three examples shown in Fig. 2, it is more instructive to plot the reflectance as a function of the film thickness,  $z$ . The film thickness is linearly related to the deposition time,  $z = \alpha t$ . The proportionality constant,  $\alpha$ , contains parameters that define the thickness of material deposited per unit time

$$\alpha = \frac{MSJ_{in} \cos \theta}{\rho N_A}, \quad (2)$$

where  $M$  is the molecular weight of deposited material,  $S$  is the condensation coefficient,  $J_{in}$  is the molecular beam flux,  $\theta$  is the angle of incidence of the molecular beam,  $\rho$  is the average density of the deposited material (i.e., including the pores), and  $N_A$  is Avogadro's number.

For all three films shown in Fig. 2, the reflectance displays oscillatory temporal behavior as expected from constructive and destructive interference.<sup>17</sup> Since the observed oscillations are sustained, the absorption in the film is negligible, indicating that the imaginary component of the index of refraction,  $k$ , is approximately zero. A dramatic decrease in the modulation of the reflectance,  $\Delta R$ , is observed for large  $\theta$ . However, since the reflectance measurements are carried out with different incident laser-beam angles,  $\phi_0$ , a direct comparison of  $\Delta R$  versus  $\theta$  is not possible. Instead, an analysis of the waveform is carried out by fitting the reflectance data versus growth time using Eq. (1) and the solution presented in the Appendix. The fitting parameters are the index of refraction,  $n$ , and the thickness,  $z$ , of the ASW film (or equivalently, the proportionality constant  $\alpha$  relating  $z$  and

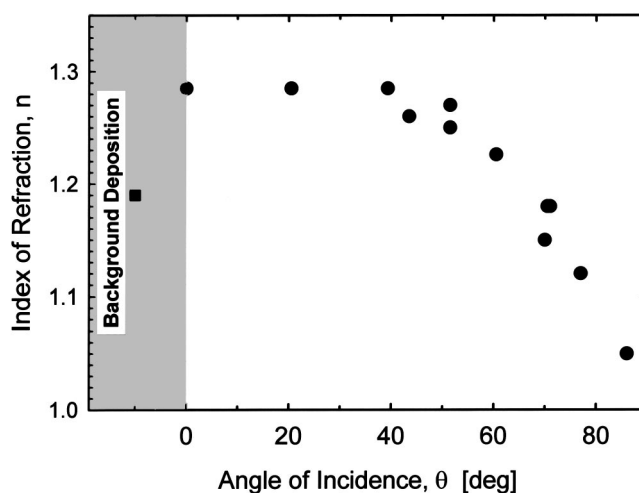


FIG. 3. Dependence of the index of refraction of ASW films on the deposition angle (solid circles). The solid square data point is obtained from ASW deposited from background  $H_2O$  vapor.

$t$ ). The solid lines in Fig. 2 represent the calculated reflectance based on the extracted fitting parameters, and exhibit excellent agreement with data.

The values of  $n$  determined from fitting the reflectance measurements are shown as a function of the deposition angle,  $\theta$ , in Fig. 3. For  $\theta \leq 40^\circ$ , the index of refraction,  $n$ , is approximately independent of the deposition angle and equal to  $1.285 \pm 0.01$ . For larger  $\theta$ ,  $n$  monotonically decreases from 1.285 to 1.050 at  $\theta = 86^\circ$  (the largest deposition angle used in these experiments). Films deposited from the background at comparable deposition rates ( $< 1$  ML/s) have  $n = 1.20$  (solid square, Fig. 3).

The density of the films can also be determined using Eq. (2) once  $\alpha$  has been obtained from fitting the reflectivity data. The experimental parameters that determine the amount of  $H_2O$  deposited in the film,  $J_{in}$ ,  $S$ , and  $\theta$ , can be independently measured. For all the experimental conditions reported here, the value of  $S$  for a quasieffusive, thermal  $H_2O$  beam was previously determined<sup>5</sup> to be  $0.99^{+0.01}_{-0.03}$ . The incident  $H_2O$  beam flux,  $J_{in}$ , is determined by measuring the time required to obtain a saturated monolayer coverage with known areal density on several substrates such as Ru(0001), and MgO(100).<sup>5,19,20</sup> For the reflectivity measurements,  $J_{in}$  was fixed at  $2.3 \times 10^{14}$   $H_2O/cm^2/s$ . We estimate that the error in determining the density associated with the combined experimental uncertainties in  $J_{in}$ ,  $S$ , and  $\theta$  is  $\pm 10\%$ . The density of the ASW films as function of the growth angle,  $\theta$ , determined using Eq. 2 is shown in Fig. 4 (open circles). The density is approximately constant for  $\theta \leq 40^\circ$  and decreases rapidly for  $\theta > 50^\circ$ . At the most oblique growth angle ( $86^\circ$ ) the density is  $0.16$   $g/cm^3$ .

As with previous optical interference studies of ASW,<sup>9</sup> the Lorentz-Lorenz relationship can also be used to relate the index of refraction,  $n$ , and the density,  $\rho$ , of the ASW films

$$\frac{\rho}{\rho_i} = \frac{n^2 - 1}{n^2 + 2} \cdot \frac{n_i^2 + 2}{n_i^2 - 1}. \quad (3)$$



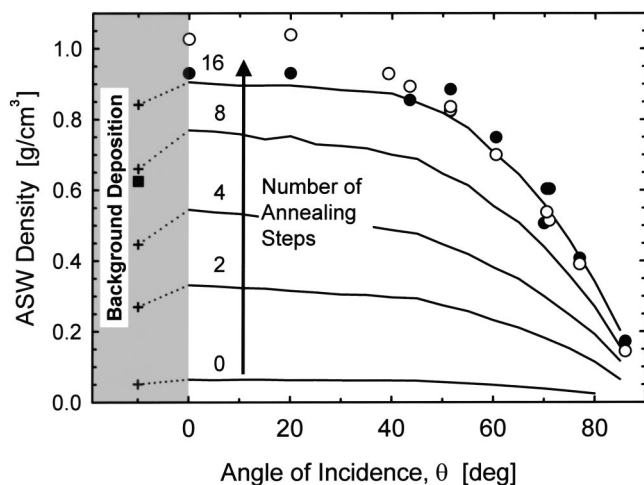


FIG. 4. ASW density vs deposition angle determined from the index of refraction (solid symbols) and the thickness (empty circles) of the ASW film. The solid square data point corresponds to ASW deposited from background  $\text{H}_2\text{O}$  vapor. Solid lines and + data points show the results of ballistic deposition simulations with different numbers (0–16) of annealing steps.

Here,  $\rho_i$  is the density of nonporous ASW (i.e., the intrinsic density) and  $\rho$  is the average density of the porous ASW.  $n_i$  and  $n$  are indexes of refraction for the nonporous and porous ASW, respectively. For the values of  $n$ , relevant for this work ( $n < 1.3$ ) Eq. (3) can be further simplified and  $\rho$  becomes a linear function of  $n$ :  $\rho @ 3.30 \times (n - 1)$ .

The validity of the Lorentz–Lorenz equation is based on two basic assumptions: (a) The film is homogeneous on the length scale set by the wavelength of the light. This requires the pores in the film to be smaller than the wavelength of the light at which  $n$  is measured (632.8 nm in these experiments). (b) The oscillator strength of  $\text{H}_2\text{O}$  in the porous and dense films needs to be the same. The legitimacy of the first assumption is supported by the fact that the constructive and destructive interference oscillations are sustained, suggesting that light scattering due to film inhomogeneities or surface roughness is negligible. The second assumption was validated previously on ASW films with low porosity by independent measurements of index of refraction and density,<sup>9</sup> and is further confirmed here for a wide range of ASW porosities.

To extract the density of porous ASW films using Eq. (3) requires knowledge of the density and index of refraction of the dense ASW films. We choose to use the previously published value<sup>4,21</sup> for dense ASW,  $\rho_i = 0.94 \text{ g/cm}^3$ , which is in agreement within the experimental uncertainty with the density determined using the procedure described above. For  $\theta = 0^\circ$ , the index of refraction for ASW is found to be  $1.285 \pm 0.01$ . We have also determined  $n$  for crystalline ice films deposited at 140 K to be  $1.285 \pm 0.01$ . This value of  $n$  for crystalline ice is independent of the deposition angle (including background deposition) and the details of the reflectance measurements (i.e.,  $s$  or  $p$  polarization, different  $\varphi_0$ ), and more importantly it is identical to the value for ASW deposited at normal angle of incidence. The absolute value of  $n = 1.285$  for crystalline ice and dense ASW compares well with previously measured values by Westley *et al.*<sup>9</sup> (1.28–

1.30) and Brown *et al.*<sup>5</sup> (1.29–1.31). At the temperatures where crystalline ice films are grown ( $T \geq 140 \text{ K}$ ), surface diffusion is fast and therefore it is quite unlikely that the crystalline ice films are not fully dense. Also, the observation that the ASW films deposited at  $\theta = 0^\circ$  have  $n$  that is identical to that of crystalline ice and independent of deposition temperature<sup>9</sup> would argue against the presence of pores in these ASW films. Therefore, we use  $n = 1.285$  as the value for  $n_i$  in the Lorentz–Lorenz relationship.

The density as function of deposition angle determined from the index of refraction using the Lorentz–Lorenz equation is shown in Fig. 4 (solid symbols). The densities obtained using the two methods are in very good agreement, suggesting that the assumptions in the Lorentz–Lorenz equation are valid in this case.

The solid lines in Fig. 4 show the density as a function of  $\theta$  obtained from our ballistic deposition simulations.<sup>1</sup> For a given angle, the density obtained in the simulation depends on the extent of surface diffusion. In the simulations, each deposited particle is allowed a certain number (0 to 16) of random diffusive steps (annealing steps) to maximize its coordination. As expected, the film density increases with increasing number of annealing steps. Simulated films for which no annealing steps are allowed are extremely porous, even at normal incidence. However, normal deposition and 16 annealing steps results in almost complete densification of the film. For the “annealed” films, the ballistic deposition simulations are in qualitative agreement with the experimentally determined  $\rho$  versus  $\theta$ .

The simulations with 16 annealing steps overestimate the density of the background deposited films. This discrepancy between the simulation and the data is not surprising given the simplicity of the model in general and its treatment of annealing in particular. In the model, the particles are only allowed to “diffuse” immediately after they strike the film and are subsequently frozen in place. Thus, the particles in the simulation might more appropriately be described as having transient mobility after adsorption. In the experiments, however, all the molecules in the film can potentially diffuse at any time during the film growth. Based on the simulations, we expect the morphology of films grown by background deposition to be significantly different than those grown with a collimated beam. Therefore, it is not surprising that the amount of annealing or “transient mobility” chosen to match the collimated beam experiments does not also match the background deposition experiment.

To illustrate how the film morphology changes with  $\theta$ , Fig. 5 shows two-dimensional sections of simulated films for a variety of deposition angles. The plane of view for the sections is defined by the incident molecular beam and the surface normal. The simulations with 16 annealing steps were selected since they display the best agreement with the experimentally determined densities. For angles smaller than  $\sim 40^\circ$  the films are almost completely dense and are nearly identical independent of  $\theta$ . A small number of relatively large pores still persist in the simulations under these deposition conditions. For larger angles of incidence filamentous structures develop. The filaments are tilted toward the incident beam. In agreement with previous ballistic deposition stud-

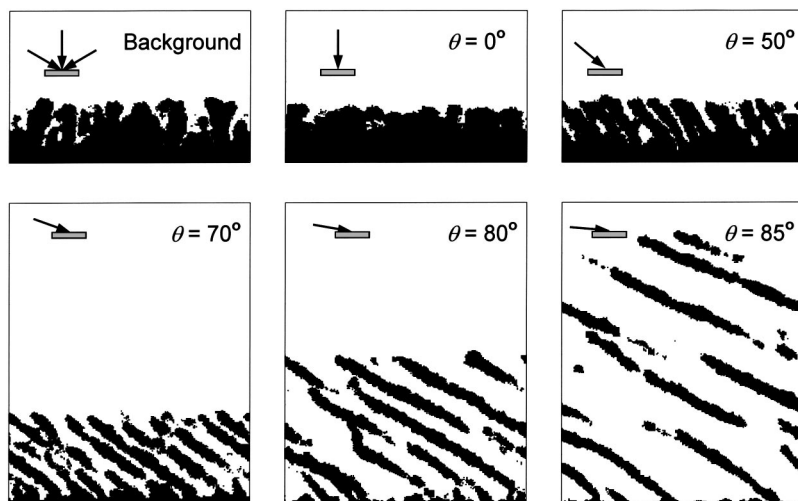


FIG. 5. Two-dimensional sections through the 50 ML films obtained from the three-dimensional ballistic deposition simulations with 16 annealing steps (see the text) at different deposition angles. The apparent presence of unattached parts of the filaments is a result of presentation of two-dimensional sections from three-dimensional simulations.

ies, the filament tilt angle is smaller than the incident angle of the growth beam.<sup>22</sup> As expected, the filament–filament spacing increases with increasing  $\theta$  since the length of shadows is proportional to the  $\tan \theta$ . In the case of background deposition the filaments are oriented normal with respect to substrate surface and have significantly bigger diameter.

Complementary information about the film morphology is provided by measurements of the specific surface area. We have employed temperature programmed desorption of gases physisorbed on ASW to determine how the ASW surface area changes with the deposition angle. The results shown here were described in our previous studies<sup>2,3</sup> but are presented here concurrently with the reflectance measurements to provide a more complete characterization of the ASW films. Briefly, the physisorption of Ar, N<sub>2</sub>, and CH<sub>4</sub> is performed at temperatures that do not allow for condensation of more than one layer of adsorbate on a flat ASW surface (26.5, 30, and 36 K for N<sub>2</sub>, Ar, and CH<sub>4</sub>, respectively). The films are dosed until the adsorption is saturated as monitored by the King and Wells technique.<sup>23</sup> For the porous films, the adsorbates readily diffuse throughout the films, condensing in small pores via capillary condensation.<sup>2,3</sup> The physisorbed gas is subsequently desorbed by linearly ramping the temperature of the substrate and measuring the desorption rate versus temperature with a QMS (temperature programmed desorption).

The integrated amount of adsorbed N<sub>2</sub>, Ar, and CH<sub>4</sub> versus the film deposition angle is shown in Fig. 6(A). The amount of gas adsorbed by porous films is normalized relative to the amount of adsorption in the first layer on dense ASW films, which we define to be 1 ML.<sup>2,3</sup> All three gases show qualitatively similar behavior as the deposition angle increases. For angles of less than 30° the amount of the adsorbed gas stays approximately constant and equal to that on dense ASW deposited at 0°. For larger angles the amount of adsorbed gas increases with increasing deposition angle, peaks at 70° to 75°, and steadily decreases as the deposition angle approaches 90°. The reflectance measurements, ballistic deposition simulations, and the fact that the maximum in the gas uptake occurs at different angles for different adsorbates all suggest that the maximum is not due to a maximum

in the surface area of the films at deposition angles of  $\sim 75^\circ$ . As mentioned above, the adsorbates can condense within the porous films due to capillary condensation. However, the extent of pore condensation is sensitive to several aspects of the experiment including the pore size distribution, the ASW film temperature during the gas adsorption, the gas flux, and physical properties of the physisorbed gas such as its surface tension.<sup>2,3</sup> For films grown at very large angles of incidence, many of the pores become too large for pore condensation to

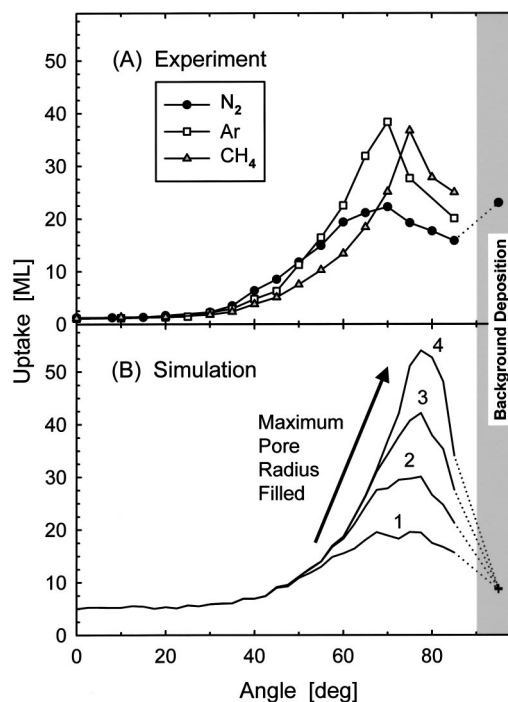


FIG. 6. (A) Integrated N<sub>2</sub>, Ar, and CH<sub>4</sub> adsorption on 50 bilayer ASW films versus the film deposition angle. The ASW films were grown at 22 K. The solid circle data point is obtained from ASW deposited from background H<sub>2</sub>O vapor. (B) Simulated integrated adsorption (including pore condensation) versus deposition angle (solid lines) for 3D, 50 ML films with 16 annealing steps. The + data points show the integrated adsorption for films grown by background dosing. In these simulations, the pore sizes are calculated and the amount of adsorption by pores less than or equal to a given maximum size is evaluated.

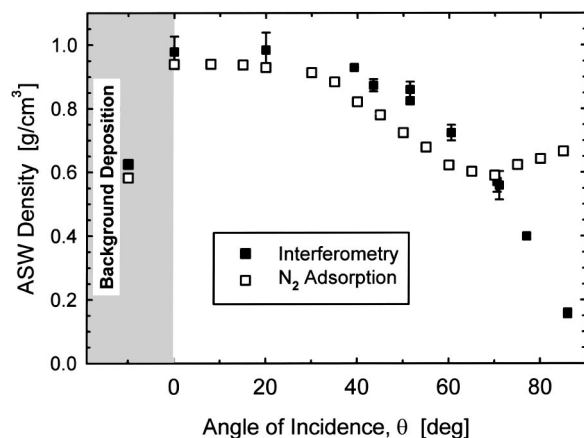


FIG. 7. The ASW density vs deposition angle. Empty squares: density calculated using the amount of  $N_2$  adsorption from Fig. 6(A) assuming complete filling of all the pores with  $N_2$ . Solid squares: density obtained by averaging the interferometric results displayed in Fig. 4.

occur under the experimental conditions. This lack of pore condensation results in a decrease in the amount of gas adsorbed by the film.

The ballistic deposition simulations also support this explanation for the maximum in the gas uptake. In the simulations, we can assess the “pore size” at any point in the porous volume and then calculate the total volume associated with pores less than some maximum size as a function of deposition angle, number of annealing steps, etc.<sup>1,3</sup> The equivalent adsorption in monolayers is then calculated from the pore volume in which condensation can occur. The simulation also includes the adsorption on the exterior surface of the film. Figure 6(B) shows the simulated adsorption due to pores smaller than a maximum radius as function deposition angle for several choices of the maximum radius. In each case, the adsorption has a maximum at large angles of incidence. As the maximum pore size for condensation is increased, the adsorption maximum becomes more pronounced and shifts to larger  $\theta$ . The “true surface area” (i.e., without pore condensation) is simulated when the maximum fill radius is set to 1. In that case, there are no significant changes in the surface area at large deposition angles ( $\theta > 65^\circ$ ). This can be related to the fact that the filamentous structure is already well developed (see Fig. 5) at that point. The main morphological change with increasing  $\theta$  is then an increase in the filament–filament separation distance, which does not appreciably change the surface area but affects the average film density dramatically.

Previously, we demonstrated that the porous network in the ASW films is highly connected, i.e., “open.”<sup>3</sup> In that case, the amount of gas adsorbed in the pores [Fig. 6(A)] can be used to estimate the volume of the pores. Knowing the volume of the pores, the amount of water deposited, and the densities of solid  $N_2$  ( $1.145 \text{ g/cm}^3$ )<sup>24</sup> and dense ASW ( $0.94 \text{ g/cm}^3$ ),<sup>4,21</sup> it is possible to estimate the density of the porous ASW films. The density as a function of growth angle, calculated using the amount of  $N_2$  adsorbed in the pores, is shown in Fig. 7 (open squares). The amount of  $N_2$  adsorbed in the pores is taken as the total amount of adsorbed  $N_2$  as shown Fig. 6(A), reduced by one  $N_2$  monolayer which is

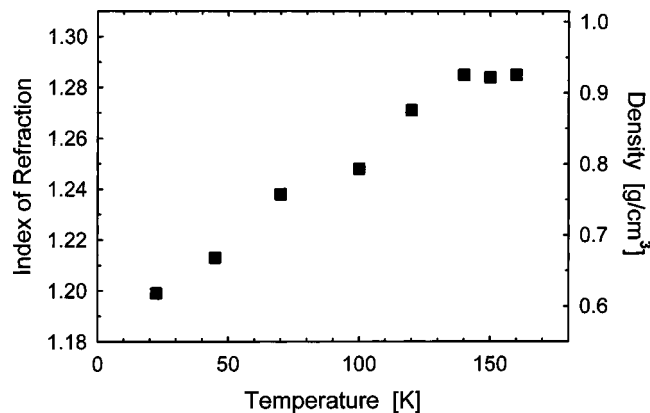


FIG. 8. The index of refraction and density of films deposited from background  $H_2O$  vapor as a function of deposition temperature.

assumed to be adsorbed on the external surface of the ASW films. Similar experiments were performed using Ar and  $CH_4$ , yielding qualitatively similar results. For clarity, these data are not displayed in Fig. 7.

For comparison, the density (filled squares) obtained by averaging the two values determined more directly from the laser interferometry measurements (see Fig. 4) is also shown in Fig. 7. For  $\theta < 60^\circ$ , the densities extracted from the gas adsorption measurements agree fairly well with the densities determined by laser interferometry, suggesting that in this range the porous network is open and completely filled by the adsorbed gas. As discussed above, for larger growth angles ( $\theta > 60^\circ$ ), the average pore size increases and the adsorbed gases can no longer condense in the largest pores. As a result, the density deduced from the amount of adsorbed gas no longer tracks the true density measured with laser interferometry.

We have also investigated the temperature dependence of both the index of refraction and density of ASW films grown by background deposition (Fig. 8). For these experiments, the sample temperature during deposition was held between 22 and 160 K. The index of refraction and the density of the films increase approximately linearly with deposition temperature between 22 and 140 K. For  $T \geq 140 \text{ K}$ , the deposited films are crystalline and both the index of refraction and the density are constant. These results are in good agreement with previously published results using similar deposition conditions.<sup>5,7</sup> Interestingly, the surface area of these background deposited films decreases more rapidly with increasing temperature than the density increases.<sup>3</sup> Already at  $\sim 90 \text{ K}$  the surface area of these films is identical to that of dense ASW. We believe that for  $90 \text{ K} < T < 140 \text{ K}$  these ASW films contain closed pores that are not connected to the external film surface.

## V. SUMMARY

Amorphous solid water (ASW) films were grown as a function of deposition angle on Mo(100) at 22 K. The specular reflectance of the ASW films was measured during the ASW growth using laser interferometry. The time-dependent reflectance was analyzed to extract the thickness and index of refraction of the film as a function of deposition angle.



The average densities (including pores) of ASW films were obtained by two methods. From the film thickness and known incident beam flux the density was determined directly. The density was also determined from the index of refraction using the Lorentz–Lorenz relationship. Within the experimental uncertainties both of these methods yield the same densities as a function of deposition angle.

At low deposition angles ( $\theta < 40^\circ$ ), the ASW density remains approximately constant and its value corresponds to that of dense ASW. At higher angles, the ASW density monotonically decreases and at  $\theta = 86^\circ$  reaches a value that is only  $\sim 17\%$  of that for dense ASW. The decrease of density with increasing angle is in good agreement with the results of ballistic deposition simulations.<sup>1</sup> These simulations illustrate the importance of shadowing in the development of porous films deposited at glancing angles.<sup>13</sup> While the density decreases monotonically with increasing deposition angle, the apparent film surface area exhibits a maximum at  $\sim 75^\circ$ .<sup>2,3</sup> The results of ballistic deposition simulations show that this apparent maximum is most likely the result of pore condensation in small pores most prevalent in films grown at intermediate deposition angles.<sup>1</sup>

## ACKNOWLEDGMENTS

This work was supported by the U.S. Department of Energy Office of Basic Energy Sciences, Chemical Sciences Division, and it was performed at the W. R. Wiley Environmental Molecular Sciences Laboratory, a national scientific user facility sponsored by the Department of Energy's Office of Biological and Environmental Research and located at Pacific Northwest National Laboratory. Pacific Northwest National Laboratory is operated for the U.S. Department of Energy by Battelle under Contract No. DE-AC06-76RLO 1830. P.A. gratefully acknowledges support from the National Science and Engineering Research Council of Canada (NSERC) for a postdoctoral fellowship.

## APPENDIX: DEFINITION AND SOLUTION OF THE PROBLEM

This Appendix describes the general solution for the reflectance,  $\mathbf{R}$ , of the bilayer system that is schematically shown in Fig. 1. This system consists of an optically flat film with a complex index of refraction,  $n-ik$ , deposited on a substrate with a complex index of refraction,  $n_s-ik_s$ . For simplicity the outer medium is considered to be vacuum with an index of refraction,  $n_0 = 1$ .

### 1. Definition of the problem

The amplitude of the reflected wave,  $R$ , is obtained by summation of all reflected rays from the substrate and the interface and is given by the following relationship:<sup>17</sup>

$$R = \frac{r_1 + r_2 e^{-2i\delta}}{1 + r_1 r_2 e^{-i2\delta}}. \quad (\text{A1})$$

Here,  $r_1$  and  $r_2$  are the Fresnel coefficients and  $\delta$  is the phase change of the light as it passes through the film. The derivation of Eq. (A1) can be found in standard textbooks on optics.<sup>17</sup> The values of the Fresnel coefficients are given by

the following equations and are dependent on the polarization of light. For  $s$  polarized light (subscript  $s$ ):

$$r_{1s} = \frac{\cos \varphi_0 - (n-ik) \cos \varphi_1}{\cos \varphi_0 + (n-ik) \cos \varphi_1}, \quad (\text{A2})$$

for  $n_0 = 1$ , and

$$r_{2s} = \frac{(n-ik) \cos \varphi_1 - (n_s-ik_s) \cos \varphi_2}{(n-ik) \cos \varphi_1 + (n_s-ik_s) \cos \varphi_2}, \quad (\text{A3})$$

where  $\varphi_0$ ,  $\varphi_1$ , and  $\varphi_2$  are the light propagation angles in the vacuum, film, and the substrate, respectively. For  $p$  polarization (subscript  $p$ ) the Fresnel coefficients are

$$r_{1p} = \frac{\cos \varphi_1 - (n-ik) \cos \varphi_0}{\cos \varphi_1 + (n-ik) \cos \varphi_0}, \quad (\text{A4})$$

for  $n_0 = 1$ , and

$$r_{2p} = \frac{(n-ik) \cos \varphi_2 - (n_s-ik_s) \cos \varphi_1}{(n-ik) \cos \varphi_2 + (n_s-ik_s) \cos \varphi_1}. \quad (\text{A5})$$

The phase change of the light passing through the film is determined by the wavelength of light,  $\lambda$ , complex index of refraction of the film,  $n-ik$ , film thickness,  $z$ , and the light propagation angle in the film,  $\varphi_1$ , via the following relationship:

$$\delta = \frac{2\pi}{\lambda} (n-ik) z \cos \varphi_1. \quad (\text{A6})$$

The film thickness is proportional to the deposition time,  $z = \alpha t$ . The proportionality constant,  $\alpha$ , is given by

$$\alpha = \frac{MSJ_{in} \cos \theta}{\rho N_A}, \quad (\text{A7})$$

where  $M$  is the molecular weight of deposited material,  $S$  is the condensation coefficient,  $J_{in}$  is the molecular beam flux,  $\theta$  is the angle of incidence of the molecular beam,  $\rho$  is the density of deposited material (including the pores), and  $N_A$  is Avogadro's number.

The light propagation angles in the vacuum, film, and the substrate are related via Snell's law

$$\sin \varphi_0 = (n-ik) \sin \varphi_1 = (n_s-ik_s) \sin \varphi_2. \quad (\text{A8})$$

### 2. Solution

The dependence of the reflectance on the film thickness and the complex indexes of refraction of the film and the substrate of this system for  $s$  and  $p$  polarized light,  $\mathbf{R} = |R|^2 = f(z, n-ik, n_s-ik_s)$ , can be obtained by algebraically solving the set of above-defined equations with complex indexes of refraction and propagation angles. The solution is presented through the following set of equations:

$$a_1 = (n^2 - k^2)^2 + 4n^2 k^2, \quad (\text{A9})$$

$$b_1 = \frac{(n^2 - k^2)(\sin \varphi_0)^2}{a_1}, \quad (\text{A10})$$

$$a_2 = (n_s^2 - k_s^2)^2 + 4n_s^2 k_s^2, \quad (\text{A11})$$



$$b_2 = \frac{(n_s^2 - k_s^2)(\sin \varphi_0)^2}{a_2}, \quad (\text{A12})$$

$$c_1 = \frac{1}{2} \sqrt{2 \sqrt{(1-b_1)^2 + 4 \frac{n^2 k^2 (\sin \varphi_0)^4}{a_1^2}} + 2 - 2b_1}, \quad (\text{A13})$$

$$d_1 = \frac{1}{2} \sqrt{2 \sqrt{(1-b_1)^2 + 4 \frac{n^2 k^2 (\sin \varphi_0)^4}{a_1^2}} - 2 + 2b_1}, \quad (\text{A14})$$

$$c_2 = \frac{1}{2} \sqrt{2 \sqrt{(1-b_2)^2 + 4 \frac{n_s^2 k_s^2 (\sin \varphi_0)^4}{a_2^2}} + 2 - 2b_2}, \quad (\text{A15})$$

$$d_2 = \frac{1}{2} \sqrt{2 \sqrt{(1-b_2)^2 + 4 \frac{n_s^2 k_s^2 (\sin \varphi_0)^4}{a_2^2}} - 2 + 2b_2}. \quad (\text{A16})$$

The following expressions depend on the polarization of the light, and the functions are labeled with  $s$  and  $p$  subscripts for  $s$  and  $p$  polarized light, respectively:

*S polarization*

$$p_{1s} = \cos \varphi_0 + n c_1 - k d_1, \quad (\text{A17})$$

$$q_{1s} = p_{1s}^2 + (-n d_1 - k c_1)^2, \quad (\text{A18})$$

$$e_{1s} = \frac{(\cos \varphi_0 - n c_1 + k d_1) p_{1s}}{q_{1s}} + \frac{(n d_1 + k c_1)(-n d_1 - k c_1)}{q_{1s}}, \quad (\text{A19})$$

$$f_{1s} = \frac{(n d_1 + k c_1) p_{1s}}{q_{1s}} - \frac{(\cos \varphi_0 - n c_1 + k d_1)(-n d_1 - k c_1)}{q_{1s}}, \quad (\text{A20})$$

$$p_{2s} = -n d_1 - k c_1 - n_s d_2 - k_s c_2, \quad (\text{A21})$$

$$q_{2s} = n c_1 - k d_1 + n_s c_2 - k_s d_2, \quad (\text{A22})$$

$$e_{2s} = \frac{(n c_1 - k d_1 - n_s c_2 + k_s d_2) q_{2s}}{p_{2s}^2 + q_{2s}^2} + \frac{(-n d_1 - k c_1 + n_s d_2 + k_s c_2) p_{2s}}{p_{2s}^2 + q_{2s}^2}, \quad (\text{A23})$$

$$f_{2s} = \frac{(-n d_1 - k c_1 + n_s d_2 + k_s c_2) q_{2s}}{p_{2s}^2 + q_{2s}^2} - \frac{(n c_1 - k d_1 - n_s c_2 + k_s d_2) p_{2s}}{p_{2s}^2 + q_{2s}^2}. \quad (\text{A24})$$

*P polarization*

$$p_{1p} = -d_1 - k \cos \varphi_0, \quad (\text{A25})$$

$$q_{1p} = c_1 + n \cos \varphi_0, \quad (\text{A26})$$

$$e_{1p} = \frac{(c_1 - n \cos \varphi_0) q_{1p}}{p_{1p}^2 + q_{1p}^2} + \frac{(-d_1 + k \cos \varphi_0) p_{1p}}{p_{1p}^2 + q_{1p}^2}, \quad (\text{A27})$$

$$f_{1p} = \frac{(-d_1 + k \cos \varphi_0) q_{1p}}{p_{1p}^2 + q_{1p}^2} - \frac{(c_1 - n \cos \varphi_0) p_{1p}}{p_{1p}^2 + q_{1p}^2}, \quad (\text{A28})$$

$$p_{2p} = -n d_2 - k c_2 - n_s d_1 - k_s c_1, \quad (\text{A29})$$

$$q_{2p} = n c_2 - k d_2 + n_s c_1 - k_s d_1, \quad (\text{A30})$$

$$e_{2p} = \frac{(n c_2 - k d_2 - n_s c_1 + k_s d_1) q_{2p}}{p_{2p}^2 + q_{2p}^2} + \frac{(-n d_2 - k c_2 + n_s d_1 + k_s c_1) p_{2p}}{p_{2p}^2 + q_{2p}^2}, \quad (\text{A31})$$

$$f_{2p} = \frac{(-n d_2 - k c_2 + n_s d_1 + k_s c_1) q_{2p}}{p_{2p}^2 + q_{2p}^2} - \frac{(n c_2 - k d_2 - n_s c_1 + k_s d_1) p_{2p}}{p_{2p}^2 + q_{2p}^2}. \quad (\text{A32})$$

For both  $s$  and  $p$  polarization, we also define

$$g_1 = 4 \frac{\pi z n c_1}{\lambda} - 4 \frac{\pi z k d_1}{\lambda}, \quad (\text{A33})$$

$$g_2 = \exp \left( -4 \frac{\pi z n d_1}{\lambda} - 4 \frac{\pi z k c_1}{\lambda} \right), \quad (\text{A34})$$

$$h_1 = (f_1 e_2 + e_1 f_2) g_2 \cos(g_1) - (e_1 e_2 - f_1 f_2) g_2 \sin(g_1), \quad (\text{A35})$$

$$h_2 = 1 + (e_1 e_2 - f_1 f_2) g_2 \cos(g_1) + (f_1 e_2 + e_1 f_2) g_2 \sin(g_1). \quad (\text{A36})$$

Using the above definitions, the reflectance is given by

$$\mathbf{R} = |\mathbf{R}|^2 = j^2 + l^2, \quad (\text{A37})$$

where

$$j = \frac{(e_1 + e_2 g_2 \cos(g_1) + f_2 g_2 \sin(g_1)) h_2}{h_1^2 + h_2^2} + \frac{(f_1 + f_2 g_2 \cos(g_1) - e_2 g_2 \sin(g_1)) h_1}{h_1^2 + h_2^2}, \quad (\text{A38})$$

$$l = \frac{(f_1 + f_2 g_2 \cos(g_1) - e_2 g_2 \sin(g_1)) h_2}{h_1^2 + h_2^2} - \frac{(e_1 + e_2 g_2 \cos(g_1) + f_2 g_2 \sin(g_1)) h_1}{h_1^2 + h_2^2}. \quad (\text{A39})$$

In Eqs. (A35) through (A39), Eq. A19 [(A27)] is substituted for  $e_1$ , Eq. (A20) [(A28)] is substituted for  $f_1$ , Eq. (A23) [(A31)] is substituted for  $e_2$ , Eq. (A24) [(A32)] is substituted for  $f_2$ , Eq. (A17) [(A25)] is substituted for  $p_1$ , Eq. (A18) [(A26)] is substituted for  $p_2$ , Eq. (A21) [(A29)] is substituted for  $q_1$ , and Eq. (A22) [(A30)] is substituted for  $q_2$ , to obtain the reflectance for  $s$  ( $p$ ) polarized light.

- <sup>1</sup>G. A. Kimmel, Z. Dohnálek, K. P. Stevenson, R. S. Smith, and B. D. Kay, *J. Chem. Phys.* **114**, 5295 (2001).
- <sup>2</sup>K. P. Stevenson, G. A. Kimmel, Z. Dohnálek, R. S. Smith, and B. D. Kay, *Science* **283**, 1505 (1999).
- <sup>3</sup>G. A. Kimmel, K. P. Stevenson, Z. Dohnálek, R. S. Smith, and B. D. Kay, *J. Chem. Phys.* **114**, 5284 (2001).
- <sup>4</sup>J. A. Ghormley and C. J. Hochanadel, *Science* **171**, 62 (1971).
- <sup>5</sup>D. E. Brown, S. M. George, C. Huang, E. K. L. Wong, K. B. Rider, R. S. Smith, and B. D. Kay, *J. Phys. Chem.* **100**, 4988 (1996).
- <sup>6</sup>B. A. Seiber, B. E. Wood, A. M. Smith, and P. R. Muller, *Science* **170**, 652 (1970).
- <sup>7</sup>B. S. Berland, D. E. Brown, M. A. Tolbert, and S. M. George, *Geophys. Res. Lett.* **22**, 3493 (1995).
- <sup>8</sup>D. R. Haynes, N. J. Tro, and S. M. George, *J. Phys. Chem.* **96**, 8502 (1992).
- <sup>9</sup>M. S. Westley, G. A. Baratta, and R. A. Baragiola, *J. Chem. Phys.* **108**, 3321 (1998).
- <sup>10</sup>A. L. Barabasi and H. E. Stanley, *Fractal Concepts in Surface Growth* (Cambridge University Press, Cambridge, 1995).
- <sup>11</sup>K. Robbie and M. J. Brett, *J. Vac. Sci. Technol. A* **15**, 1460 (1997).
- <sup>12</sup>J. C. Sit, D. Vick, K. Robbie, and M. J. Brett, *J. Mater. Res.* **14**, 1197 (1999).
- <sup>13</sup>Z. Dohnálek, G. A. Kimmel, D. E. McCready, J. S. Young, A. Dohnalkova, R. S. Smith, and B. D. Kay, *J. Phys. Chem. B* **106**, 3526 (2002).
- <sup>14</sup>H. Schlichting and D. Menzel, *Rev. Sci. Instrum.* **64**, 2013 (1993).
- <sup>15</sup>The Knudsen number (ratio of gas mean free path and nozzle diameter), Kn, of our water beam source is  $\sim 0.1$  which falls into the transition range between effusive ( $Kn \geq 1$ ) and supersonic ( $Kn < 0.01$ ) beams. The beam properties are close to that of effusive beams having nearly thermal velocity distribution and no clustering.
- <sup>16</sup>Z. Dohnálek, R. L. Ciolli, G. A. Kimmel, K. P. Stevenson, R. S. Smith, B. D. Kay, *J. Chem. Phys.* **110**, 5489 (1999).
- <sup>17</sup>O. S. Heavens, *Optical Properties of Thin Solid Films* (Dover, New York, 1991).
- <sup>18</sup>V. P. Zhdanov and P. R. Norton, *Surf. Sci.* **449**, L228 (2000).
- <sup>19</sup>M. J. Stirniman, C. Huang, R. S. Smith, S. A. Joyce, and B. D. Kay, *J. Chem. Phys.* **105**, 1295 (1996).
- <sup>20</sup>D. Ferry, A. Glebov, V. Senz, J. Suzanne, J. P. Toennies, and H. Weiss, *Surf. Sci.* **377–379**, 634 (1997).
- <sup>21</sup>A. H. Narten, C. G. Venkatesh, and S. A. Rice, *J. Chem. Phys.* **64**, 1106 (1976).
- <sup>22</sup>A. G. Dirks and H. J. Leamy, *Thin Solid Films* **47**, 219 (1977).
- <sup>23</sup>D. A. King and M. G. Wells, *Surf. Sci.* **29**, 454 (1972).
- <sup>24</sup>*CRC Handbook of Chemistry and Physics*, 80th ed. (CRC, New York, 1999).